Tat Khoa DOAN[1],
Trung Thanh NGUYEN[1],
An-Le VAN[2*]

MULTI-OBJECTIVE OPTIMIZATION OF THE ROTARY TURNING OF HARDENED MOLD STEEL FOR ENERGY SAVING AND SURFACE ROUGHNESS IMPROVEMENTS

In this investigation, the specific cutting energy (*SCE*) and average surface roughness (*R_a*) were decreased using the hard-rotary turning (HRT) factors, including the inclined angle (*I*), depth of cut (*D*), feed rate (*f*), and spindle speed (*S*). The Bayesian regularized feed-forward neural network was applied to develop the *SCE* and *R_a* models. The entropy method and vibration and communication particle swarm optimization (VCPSO) algorithm were employed to compute the weights and determine optimal factors. The optimizing outcomes presented that the optimal *I*, *D*, *f*, and *S* were 35 deg., 0.45 mm, 0.50 mm/rev., and 1200 rpm, respectively, while the *SCE* and *R_a* were decreased by 37.4% and 6.6%, respectively. The total turning cost was saved by 7.5% at the selected solution. The valuable outcomes could be applied to the practical HRT process to decrease performance measures, while the developed HRT operation could be utilized for machining difficult-to-cut materials.

1. INTRODUCTION

The rotary turning process is widely applied to cut hardened steels in terms of the production rate and quality indicators. This operation offers several benefits, including low cutting temperature, even temperature distribution, low machining force, and high tool life. Different rotary turning operations have been optimized to enhance technological parameters. A simulation model was developed to precisely capture the machining temperature in terms of the depth of cut (*D*), feed rate (*f*), and turning speed (*V*) [1]. Kishawy and Wilcox emphasized that the rotary turning process provided a high resistance and long tool life, while only the flank wear was produced [2]. A new flank wear model of the rotary turning operation was developed, while the genetic algorithm was used to find the empirical coefficients [3]. The surface roughness of 0.5 μm for the aerospace alloy could

---

be obtained using the rotary turning operation [4]. The predictive models of the turning force components of the carbon steel were developed in terms the *V*, *D*, *f*, and *A* [5]. Li et al. Indicated that an increased *V* could be used to decrease the coefficient and the turning force was primarily affected by the *f* [6]. Ezugwu stated that the machining force components of the rotary turning operation were smaller than the fixed process, while a higher *f* decreased the surface quality [7]. Rao et al. stated that the average roughness (R_a) was decreased by 14.5% at the same material removal rate for the rotary turning of EN24 steel using the genetic algorithm [8]. Amini and Teimouri indicated that the *V* of 4 m/min, the *D* of 0.3 mm, and the f of 0.08 mm/rev could be applied to minimize the cutting forces and *Ra* for the rotary turning of the AA7075 [9]. The energy consumption in the turning state (E_t), machining rate, and R_a models of the rotary turning process of the hardened steel were enhanced by 50.3%, 33.2%, and 19.8%, respectively using optimal *V*, *A*, *f*, and *D* [10]. The energy consumption and cost were saved by 9.2% and 1.37%, respectively using the optimal rotary turning variables [11]. The machining force components and temperature of the 51200 hardened steel were precisely predicted using a simulation model [12].

Ahmed et al. pointed out that the R_a of 0.38 μm and the tool wear of 2.42 μm could be obtained using optimal parameters for rotary turning AISI 4140 steel [13]. Nieslony et al. revealed that a higher *V* in the rotary turning process caused a decreased *Ra* and stable machining [14]. The minimum quantity lubrication and nano lubricant were applied to decrease the cutting temperature of the rotary milling Inconel 625 [15]. The authors stated that higher values of the *f* and *V* increased the machining temperature. A novel simulation model of the rotary turning operation was developed to predict the cutting temperature, force components, and chip morphology [16]. A good agreement between the predictive and experimental results indicated that the developed model was reliable and useful. Ahmed et al. emphasized that the rotary turning process provided lower cutting forces, flank wear, and cutting temperature, as compared to the fixed turning, while a better R_a could be obtained using the conventional one [17]. Umer et al. revealed that lower values of the *D* and *A* could be applied to decrease the turning temperature, force, and stress of the tool [18]. However, the predictive model of the *SCE* in the turning stage has not been developed and evaluated. The optimal factors for simultaneously decreasing the *SCE* and R_a of the rotary turning process have not been selected. The comprehensive cost for the rotary turning process has not been proposed in published works.

In this paper, we present the optimization approach and experiment setting for the rotary turning process of the hardened steel. Next, the obtained results are scientifically discussed. Finally, conclusions are drawn and future research is suggested.

2. OPTIMIZATION APPROACH

The concept of the hard-rotary turning (HRT) operation is shown in Fig. 1. The round insert having high hardness (87–92 HRC) is rotated using the friction between its body and the workpiece (Fig. 1a). The designed and fabricated self-propelled rotary tool has seven components, including the shank, the base, the round insert, adjusting bolts, adjusting screws, and the drive shaft (Fig. 1b). The SKD11 steel is utilized to fabricate the shank,

the base, and shaft. The base is tightly clamped on the shank using screws, while the round insert is fixed on the drive shaft. The shaft is rotated around its axis with the support of the bearing. The inclined angle is adjusted using the milled groves on the base. The MITSUBISHI carbide round insert entitled RPMT1204M0E-JS having the rake angle of 11° is applied in all tests. The outside diameter, inside diameter, and thickness of the round insert are 12 mm, 4.4 mm, and 4.76 mm, respectively (Fig. 1c).
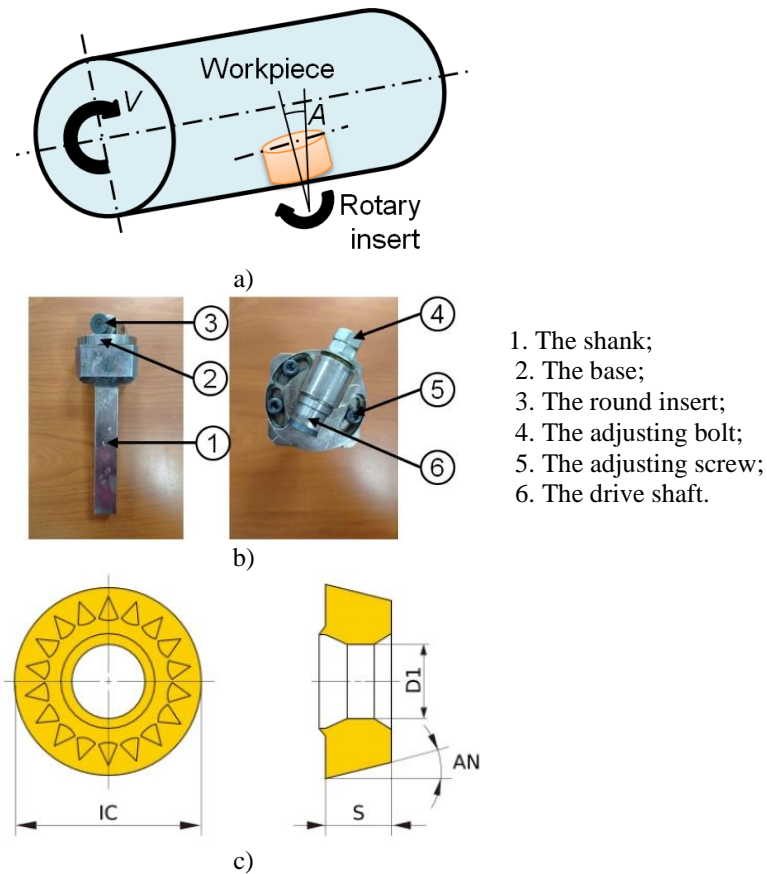

Fig. 1. The concept of the HRT process: a) – the schematic principle, b) – the fabricated rotary tool, c) – the round insert

The specific cutting energy (*SCE*) is defined as a ratio of the energy consumed in the HRT process (*TE*) and material removal volume (*MRV*) and is computed as:

$$SCE = \frac{TE}{MRV} \tag{1}$$

The *MRV* is computed as:

$$MRV = V \times f \times D \times t_c \tag{2}$$

where the *V*, *f*, *D*, and t_c are the turning speed, feed rate, depth of cut, and turning time, respectively.

The *TE* of the HRT process consists of six parts, including the startup (E_s), the standby (E_{st}), transition (E_{ts}), air-turning (E_a), turning (*EC*), and tool change (E_{tc}) stages (Fig. 2). Therefore, the *TE* model can be expressed as:

$$TE = E_s + E_{st} + E_{ts} + E_a + EC + E_{tc} \tag{3}$$

Practically, the E_{st}, E_{ts}, E_a, and E_{tc} are constant values. In this investigation, the energy consumption in the turning stage is considered; hence, the SCE is expressed as:

$$SCE = \frac{EC}{MRV} = \frac{P_c \times t_c}{MRR \times t_c} = \frac{P_c}{MRR} \tag{4}$$

where P_c is the power consumed in the turning stage.

The R_a is computed as:

$$R_a = \sum_{i=1}^{n} \frac{R_{ai}}{n} \tag{5}$$

where R_{ai} is the average roughness at the i_{th} measured position.

In the current work, the properties of the cutting insert and workpiece are considered as constants. Four key factors having the ranges, including the inclined angle, depth of cut, feed rate, and spindle speed are exhibited in Table 1. The parameter levels are identified based on the characteristics of the machine tool and the recommendations of the manufacturer of the round insert. These ranges are confirmed by the suggestions from the aforementioned works.
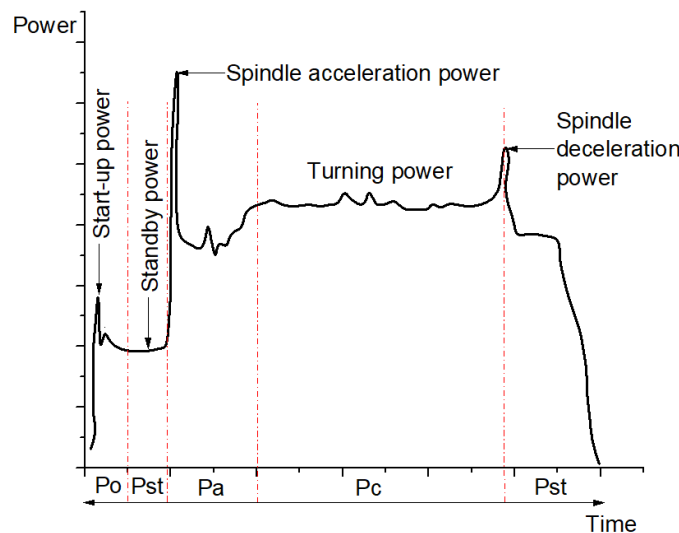
Fig. 2. The power profile of the HRT operation

Table 1. Optimizing process factors

Symbol	Parameters	Ranges
I	Inclined angle (deg.)	20-35-50
D	Turning depth (mm)	0.2-0.4-0.6
f	Feed rate (mm/rev.)	0.3-0.5-0.7
S	Spindle speed (RPM)	800-100-1200

The optimization issue is expressed as:

Find $X = [I, D, f,$ and $S]$;

Minimizing SCE and R_a;

Constraints: $20 \leq I \leq 50$ (deg.); $0.2 \leq D \leq 0.6$ (mm); $0.3 \leq f \leq 0.7$ (mm/rev.);

$800 \leq S \leq 12000$ (rpm).

The optimization procedure is shown in Fig. 3.

Step 1: Performing turning experiments using the Box-Behnken design [19]. When four turning variables and two replications are utilized, 26 experiments are required.

Step 2: The *SCE* and R_a models are developed regarding process parameters by means of the BRFFNN approach [20].

For the BRFFNN, the weights of the network are random variables. The probability density function is expressed as:

$$P = \frac{P(D|w, \beta, M)P(w|\alpha, M)}{P(D|\alpha, \beta, M)} \tag{6}$$

where D and M present the obtained data and the forward multi-layer perceptron, respectively. w and $P(w|\alpha,M)$ are the vector and prior knowledge of network weights, respectively. When the Gaussian function is employed, the like hood-P (D/w, β, M) is expressed as:

$$P(D|w, \beta, M) = \frac{1}{\left(\dfrac{\pi}{\beta}\right)^{n/2}} e^{-\beta d_d} \tag{7}$$

where d_d is the sum of squared deviations for data.

The normalized factor P ($D|\alpha$, β, M) is expressed as:

$$P(D|\alpha, \beta, M) = \frac{1}{\left(\dfrac{\pi}{\alpha}\right)^{N/2}} e^{-\alpha d_w} \tag{8}$$

where d_w is the sum of squared errors for the weights.

The probability density function is expressed as:

$$P = \frac{1}{Z_F(\alpha, \beta)} e^{-(\beta d_d + \alpha d_w)} \tag{9}$$

The highest value of the probability density function maximizes the regularized objective function ($f = \beta d_d + \alpha d_w$). The input variables are considered as probability density functions for the hidden layer. The BRFFNN approach eliminates the uncertainty related to network weights; hence, the prediction precision increases.

To observe the optimal architecture of the BRFFNN model, the operating factors, including the number of neurons in each layer, performance function, transfer function, number of hidden layers, and learning functions are optimized and selected. The numerical experiments of each ANN model are executed to calculate the mean square error (*MSE*), which is expressed as:

$$MSE = \frac{1}{N} \Sigma_{i=1}^{N} (y_a - y_p)^2 \tag{10}$$

where y_a and y_p are the actual and predictive values, respectively. N denotes the number of testing points.

The best BRFFNN architecture is chosen with the lowest MSE value.

Step 3: The weight of each response is computed using the Entropy method.

The normalized value of each response (n_{ij}) is calculated as:

$$n_{ij} = \frac{r_{ij}}{\sum_{i=1}^{m} r_{ij}} \tag{11}$$

where r_{ij} presents the response value.

The entropy outcome of each response (ET_j) is calculated as:

$$ET_j = -\frac{\sum_{j=1}^{m} n_{ij} \times \ln n_{ij}}{\ln m} \tag{12}$$

where m is the number of responses.

The computed weight of each response (ω_i) is calculated as:

$$\omega_i = \frac{1 - E_j}{\sum_{j=1}^{n}(1 - E_j)} \tag{13}$$

Step 4: Determination of the optimal HRT parameters using the VCPSO.

To obtain global optimization results, the mutation, crossover, and selection operations will be added to the VCPSO. Fig. 4 presents the sequential steps of the VCPSO.

The particle position in the mutation operation is expressed as:

$$x_i = x_{c_a} + f(x_{c_b} - x_{c_c}) \tag{14}$$

where c_a, c_b, and c_c are the random integers. The f is the scaling coefficient.

The diversity of the population is improved in the crossover operation and expressed as:

$$d_{i,d} = \begin{cases} x_{i,d} \, if \, (rand < R_C) \\ x_{i,d} \, otherwise \end{cases} \tag{15}$$

where R_c presents the percentage of the crossover.

The best particle is determined in the selection operation and expressed as:

$$p_{i,d} = \begin{cases} x_{i,d} \, if \, (f(u_i) < f(x_i)) \\ x_{i,d} \, otherwise \end{cases} \tag{16}$$

The position (x_{id}) and velocity (v_{id}) of each particle is presented as:

$$x_{id}^{n+1} = x_{id}^{n} + v_{id}^{n+1} \tag{17}$$

$$v_{id}^{n+1} = \omega v_{id}^{n} + c_1 r_1 (P_{id}^{n} - x_{id}^{n}) + c_2 r_2 (P_{gd}^{n} - x_{id}^{n}) + c_3 r_3 (P_{cd}^{n} - x_{id}^{n}) \tag{18}$$

where c_3 denotes the accelerated coefficient. The r_1, r_2, and r_3 are random numbers.

The best position of each particle is presented as:

$$x_{gbest,d}^{n+1} = x_{gbest,d}^{n} + x_{gbest,d}^{n}(rand - 0.5) \tag{19}$$
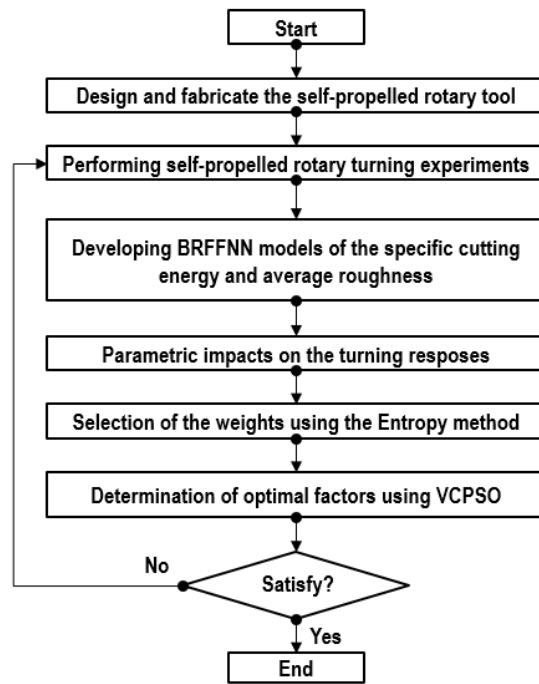
Fig. 3. Optimizing procedure
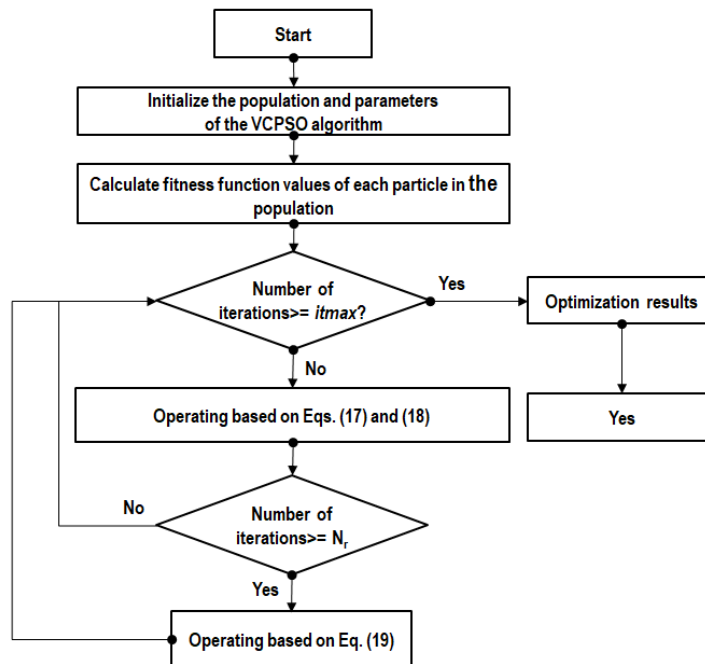
Fig. 4. Operating procedure of the VCPSO

3. EXPERIMENTAL SETTING

The cylindrical bar SKD61 having a diameter of 44 mm and length of 360 mm is chosen as an experimental specimen. The workpiece having a hardness of 56 HRC is

selected because of the applications in the fabrication of mould pins. The chemical compositions of the SKD61 are presented in Table 2.

Table 2. Chemical compositions of the SKD61

Elements	C	Si	Mn	P	S	Cr	Mo	V
%	0.40	0.9	0.35	0.03	0.02	4.0	1.2	1.2

| Power meter | Turning machine | Roughness tester |
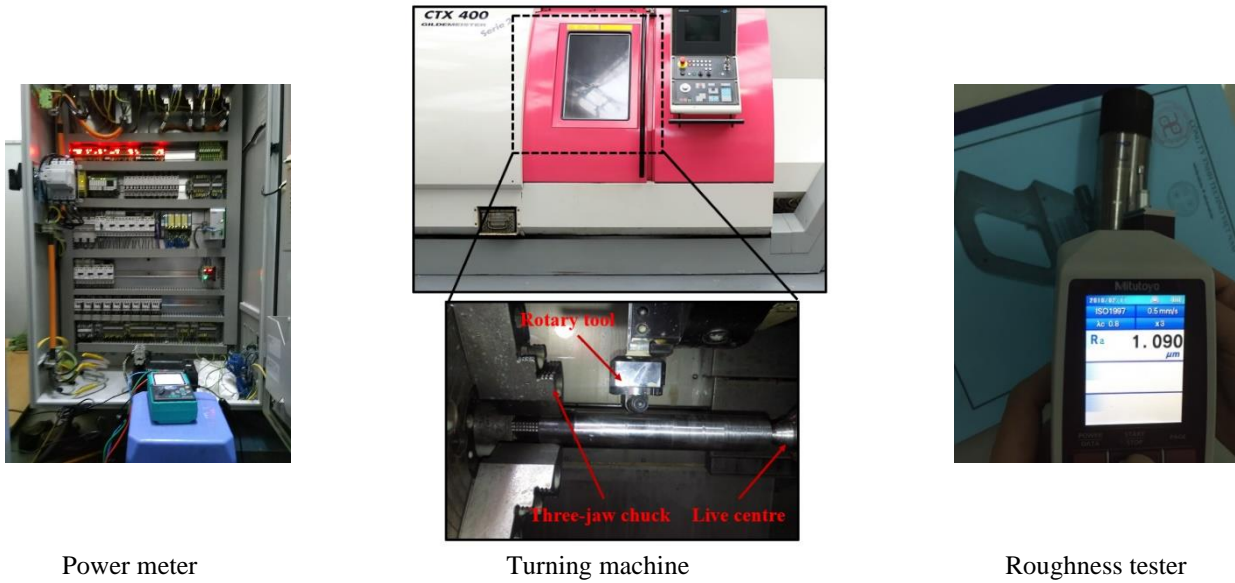
Fig. 5. Experimental setting for the HRT process
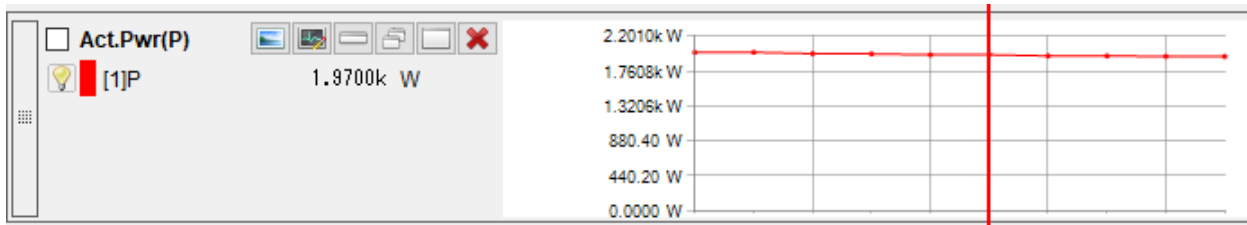
(a)
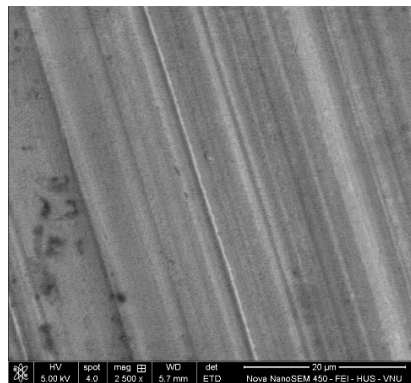
(b)

Fig. 6. Turning responses at the different process inputs: a) – The power consumed at experimental No. 19, b) – The SEM image of the turned surface at experimental No. 19

All turning experiments are performed using a CNC lathe entitled GILDEMEISTER CTX 400 Serie 2 (Fig. 5). A power meter labeled KEW6305 is employed to capture power components during the rotary turning. An interval of 0.1 sec. is used to improve the accuracy of the measured data. A roughness tester labeled SJ- 210 is used to measure the roughness in five investigated points. The sampling length of 4 mm is used to ensure the measuring precision. The example results of the turning experiments are shown in Fig. 6.

4. RESULTS AND DISCUSSIONS

4.1. DEVELOPMENT OF *SCE* AND R_a MODELS

Table 3 presents the experimental outcomes. The operating parameters of the BRFFNN model, including the *NH*, *PF*, *TF*, *NL*, and *LF* are shown in Table 4. The computational trials of the BRFFNN are performed based on the parameter combination entitled Taguchi L$_{18}$. The obtained results of the *MSE* values are shown in Table 5. As a result, the optimal data of the *HN*, *PM*, *TF*, *HL*, and *LF* are 24, MSEREG, logsig, 3, and LearnGDM, respectively (Fig. 7).
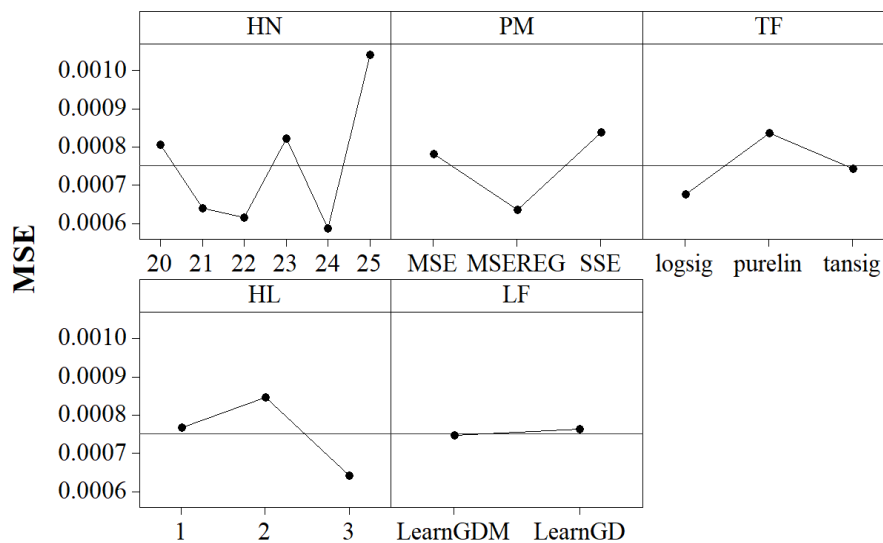
Fig. 7. The MSE values with different operating parameters

To confirm the precision of the developed ANN model, the comparisons between the experimental and predictive results are conducted. Table 6 indicates the comparative values at different points. As a result, the computed deviations of the *SC* and R_a lie from –0.73% to 0.73% and –1.65% to 1.52%, respectively. The small errors revealed that the proposed models ensure the prediction accuracy.

The regression plots of the BRFFNN are depicted in Fig. 8, in which the R values of the training, testing, and all stages are 00.98695, 0.96388, and 0.98557, respectively. Consequently, the developed BRFFNN models can approximate the function accurately. Figure 9 presents the structure of the developed BFRNN models.
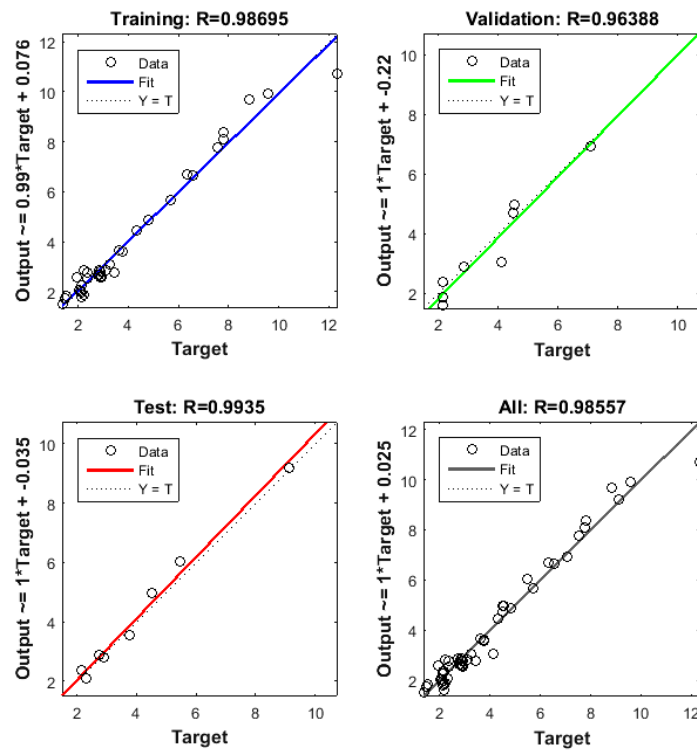
Fig. 8. Regression plots produced by the BRFFNN models
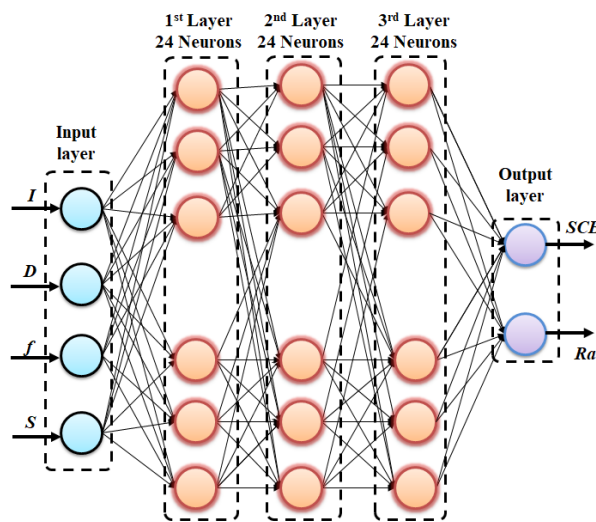
Fig. 9. The structure of the BFRNN models

Table 3. Experimental data of the rotary turning operation

No.	I (deg.)	D (mm)	f (mm/rev.)	S (rpm)	SCE (J/mm^3)	R_a (µm)
Experimental outcomes for developing BRFFNN models						
1	20	0.4	0.5	1200	4.31	2.15
2	35	0.6	0.5	800	3.76	2.73
3	50	0.4	0.3	1000	7.54	2.15
4	20	0.6	0.5	1000	3.27	2.84

5	35	0.6	0.5	1200	2.92	2.11
6	35	0.6	0.7	1000	2.38	2.78
7	20	0.4	0.3	1000	7.09	2.16
8	35	0.2	0.5	800	9.58	2.35
9	35	0.4	0.3	800	7.81	2.03
10	50	0.6	0.5	1000	3.42	2.83
11	20	0.2	0.5	1000	8.84	2.23
12	35	0.4	0.7	800	4.12	2.86
13	50	0.4	0.5	800	5.71	2.88
14	35	0.4	0.5	1000	4.52	2.17
15	35	0.4	0.7	1200	3.12	1.94
16	20	0.4	0.5	800	5.47	2.92
17	35	0.2	0.7	1000	6.33	2.21
18	20	0.4	0.7	1000	3.63	2.87
19	35	0.6	0.3	1000	4.81	2.08
20	35	0.4	0.3	1200	6.56	1.36
21	35	0.2	0.5	1200	7.78	1.46
22	35	0.4	0.5	1000	4.53	2.15
23	50	0.2	0.5	1000	9.11	2.31
24	50	0.4	0.7	1000	3.77	2.91
25	50	0.4	0.5	1200	4.49	2.16
26	35	0.2	0.3	1000	12.31	1.52
Experimental outcomes for testing the accuracy of developed BRFFNN models						
27	25	0.3	0.4	900	8.02	2.21
28	30	0.5	0.6	1100	2.73	2.31
29	40	0.3	0.5	1050	6.15	1.97
30	45	0.6	0.7	1200	2.71	2.53
31	50	0.3	0.6	950	8.15	1.79
32	40	0.5	0.4	1200	4.12	1.82

Table 4. Operating parameters of the BRNN model

Symbol	Operating inputs	Ranges
NH	Number of hidden neurons	20; 21; 22; 23; 24; 25
PF	Performance function	MSE; MSEREG; SSE
TF	Transfer function	Logsig; Purelin; Tansig
NL	Number of hidden layers	1; 2; 3
LF	Learning function	LearnGDM; LearnGD

Table 5. Computing the MSE values

No.	*NH*	*PF*	*TF*	*NL*	*LF*	*MSE*
1	20	MSE	Logsig	1	LearnGDM	0.0009470
2	20	MSEREG	Purelin	2	LearnGD	0.0007530

3	20	SSE	Tansig	3	LearnGDM	0.0007180
4	21	MSE	Logsig	2	LearnGD	0.0006717
5	21	MSEREG	Purelin	3	LearnGDM	0.0006165
6	21	SSE	Tansig	1	LearnGDM	0.0006261
7	22	MSE	Purelin	1	LearnGDM	0.0005858
8	22	MSEREG	Tansig	2	LearnGDM	0.0006296
9	22	SSE	Logsig	3	LearnGD	0.0006252
10	23	MSE	Tansig	3	LearnGD	0.0006713
11	23	MSEREG	Logsig	1	LearnGDM	0.0005889
12	23	SSE	Purelin	2	LearnGDM	0.0012040
13	24	MSE	Purelin	3	LearnGDM	0.0005842
14	24	MSEREG	Tansig	1	LearnGD	0.0005868
15	24	SSE	Logsig	2	LearnGDM	0.0005896
16	25	MSE	Tansig	2	LearnGDM	0.0012230
17	25	MSEREG	Logsig	3	LearnGDM	0.0006348
18	25	SSE	Purelin	1	LearnGD	0.0012670

Table 6. Confirmations of the precision of the developed models

No.	SCE (J/mm3)			R_a (µm)		
	Exp.	Pred.	Err.	Exp.	Pred.	Err.
27	8.02	8.04	-0.25	2.21	2.23	-0.90
28	2.73	2.71	0.73	2.31	2.29	0.87
29	6.15	6.12	0.49	1.97	1.94	1.52
30	2.71	2.69	0.74	2.53	2.55	-0.79
31	8.15	8.12	0.37	1.79	1.81	-1.12
32	4.12	4.15	-0.73	1.82	1.85	-1.65

4.2. ANOVA RESULTS

The ANOVA results of the SCE are shown in Table 7. Significant parameters are single factors (I, D, f, and S), interactive factors (Df and DS), and quadratic factors (I^2, D^2, f^2, and S^2) (Fig. 10a). The contributions of the I, D, f, and S are 1.31%, 30.35%, 20.73%, and 6.63%, respectively. The contributions of the Df and DS are 9.68% and 2.66%, respectively. The contributions of the I^2, D^2, f^2, and S^2 are 3.39%, 14.13%, 7.26%, and 13.2%, respectively. The values of the R^2 value (0.9784), the adjusted R^2 (0.9684), and the predicted R^2 (0.9562) indicate that the SCE model is adequate.
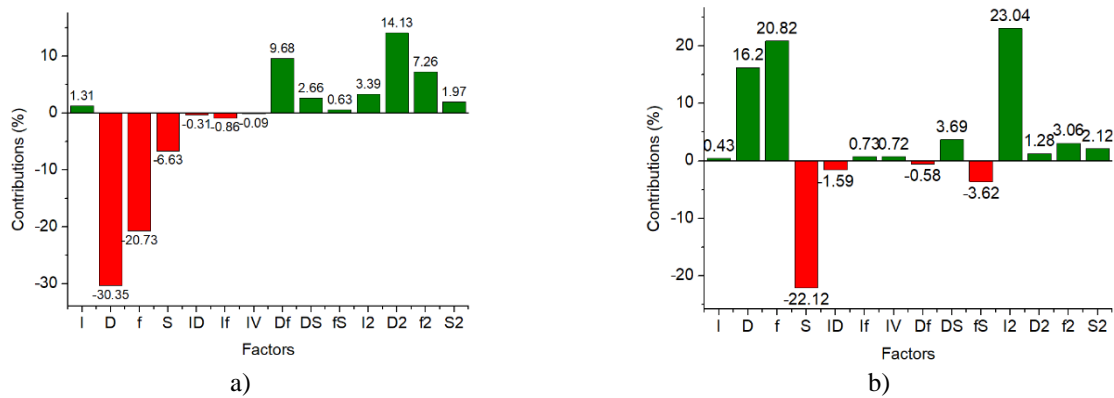
Fig. 10. Parametric contributions for turning responses: a) – for *SCE* model. b) – for R_a model

The ANOVA results of the R_a are shown in Table 8. Significant parameters are single factors (*D*, *f*, and *S*), interactive factors (*ID*, *DS*, and *fS*), and quadratic factors (I^2, D^2, f^2, and S^2) (Fig. 10b). The contributions of the *D*, *f*, and *S* are 16.2%, 20.82%, and 22.12%, respectively. The contributions of the *ID*, *DS*, and *fS* are 1.59%, 3.69%, and 3.62%, respectively. The contributions of the I^2, D^2, f^2, and S^2 are 23.04%, 1.28%, 3.06%, and 2.12%, respectively. The values of the R^2 value (0.9763), the adjusted R^2 (0.9652), and the predicted R^2 (0.9582) indicate that the R_a model is adequate.

Table 7. ANOVA results for the *SCE* model

Source	Sum of Squares	Mean Square	F-value	p-value	Remark	Contribution (%)
Model	149.4020	10.6716	31.1539	< 0.0001	Significant	
I	20.6606	20.6606	60.3229	0.0286	Significant	1.31
D	478.6637	478.6637	1397.5583	< 0.0001	Significant	30.35
f	326.9423	326.9423	954.5761	< 0.0001	Significant	20.73
S	104.5648	104.5648	305.2986	< 0.0001	Significant	6.63
ID	4.8892	4.8892	14.2749	0.7597	Insignificant	0.31
If	13.5635	13.5635	39.6013	0.404	Insignificant	0.86
IV	1.4194	1.4194	4.1443	0.873	Insignificant	0.09
Df	152.6677	152.6677	445.7451	< 0.0001	Significant	9.68
DS	41.9521	41.9521	122.4878	0.0162	Significant	2.66
fS	9.9360	9.9360	29.0103	0.5076	Insignificant	0.63
I^2	53.4652	53.4652	156.1029	0.0072	Significant	3.39
D^2	222.8507	222.8507	650.6589	< 0.0001	Significant	14.13
f^2	114.5008	114.5008	334.3088	< 0.0001	Significant	7.26
S^2	31.0698	31.0698	90.7147	0.0348	Significant	1.97
Residual	3.7680	0.3425				
Total	153.17					
R^2 = 0.9754; Adj. R^2 = 0.9684; Pred. R^2 = 0.9562						

Table 8. ANOVA results for the *Ra* model

Source	Sum of Squares	Mean Square	F-value	p-value	Remark	Contribution (%)
Model	5.2134	5.2134	453.1350	< 0.0001	Significant	
I	0.1904	0.1904	16.5595	0.5829	Significant	0.43
D	7.1745	7.1745	623.8701	< 0.0001	Significant	16.20
f	9.2206	9.2206	801.7886	< 0.0001	Significant	20.82
S	9.7963	9.7963	851.8523	< 0.0001	Significant	22.12
ID	0.7042	0.7042	61.2317	0.2338	Insignificant	1.59
If	0.3233	0.3233	28.1127	0.4985	Insignificant	0.73
IV	0.3189	0.3189	27.7276	0.4985	Insignificant	0.72
Df	0.2569	0.2569	22.3361	0.8912	Insignificant	0.58
DS	1.6342	1.6342	142.1037	0.003	Significant	3.69
fS	1.6032	1.6032	139.4080	0.005	Significant	3.62
I^2	10.2037	10.2037	887.2819	< 0.0001	Significant	23.04
D^2	0.5669	0.5669	49.2934	0.1783	Insignificant	1.28
f^2	1.3552	1.3552	117.8421	0.0172	Significant	3.06
S^2	0.9389	0.9389	81.6423	0.0486	Significant	2.12
Residual	0.1266	0.0115				
Total	5.34					
$R^2 = 0.9763$; Adj. $R^2 = 0.9652$; pred. $R^2 = 0.9582$						

4.3. PARAMETRIC INFLUENCES

As shown in Fig. 11a, the *SCE* is decreased by 1.4% with an increment in the *I* (from 20 to 30 deg). A further *I* (from 30 deg to 50 deg), the *SCE* is increased by 4.5%. A higher inclined angle decreases the contact area between the insert and the workpiece, leading to a low material volume; hence, the *SCE* decreases. A further angle increases the contact area due to the perpendicular direction between the cutting tool and workpiece, leading to a higher material volume; hence, the *SCE* increases.

As shown in Fig. 11b, the *SCE* is decreased by 64.5% with an increment in the *D* (from 0.2 to 0.6 mm). A higher *D* increases the thickness of the chip; hence, higher energy is required. Additionally, an increased *D* causes greater resistance, resulting in higher energy consumed. Unfortunately, the *SCE* is inversely proportional to the increase in the *D*; hence, the *SCE* decreases.

As shown in Fig. 11c, the *SCE* is decreased by 46.8% with an increment in the *f* (from 0.3 to 0.7 mm/rev.). A higher *f* decreases the turning time; hence, the *SCE* consequently decreases with a higher *f*.

As shown in Fig. 11d, the *SCE* is decreased by 13.5% with an increment in the *S* (from 800 to 1200 rpm). A higher *S* decreases the hardness and strength of the workpiece due to increasing machining temperature; hence, the *SCE* reduces. Additionally, a higher *S* decreases the turning time; hence, the *SCE* decreases.
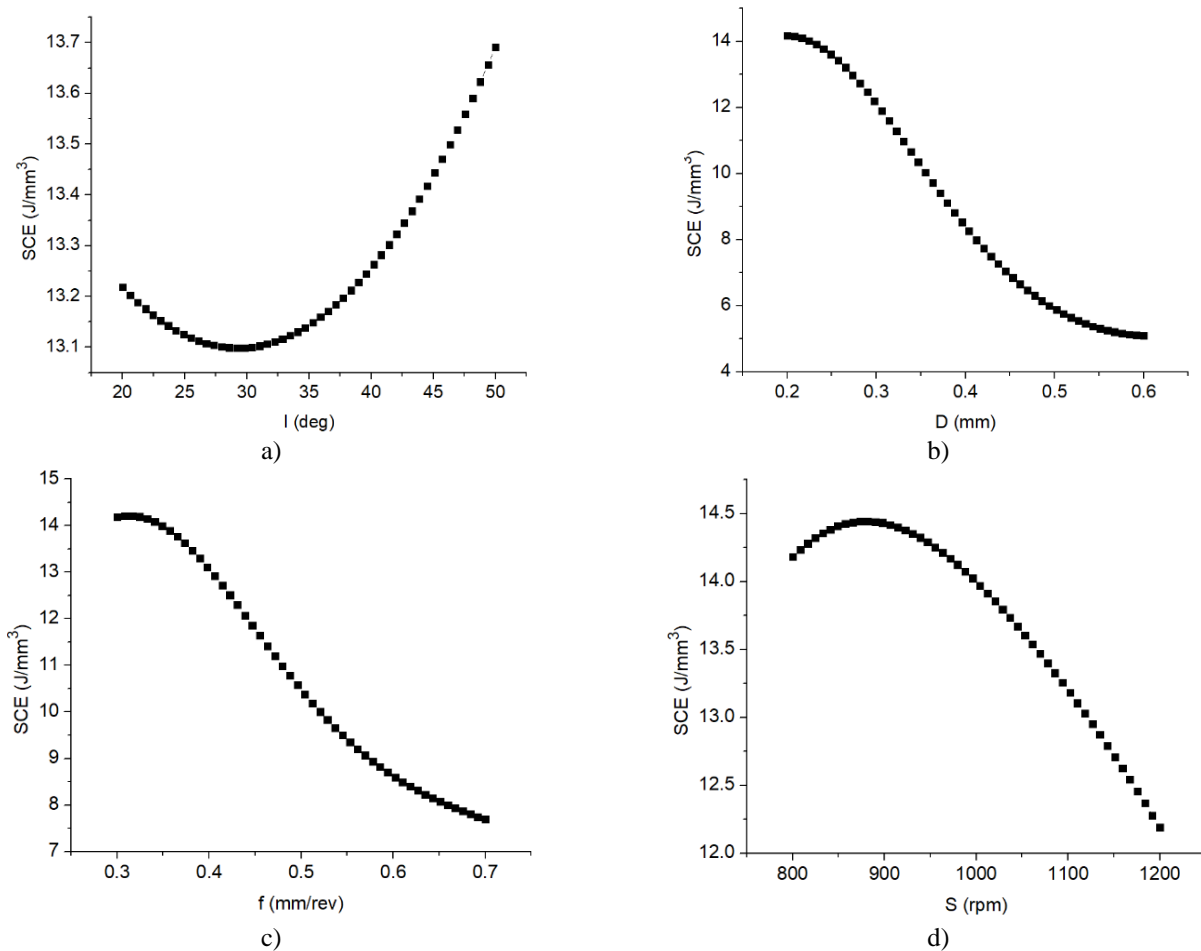
Fig. 11. The impacts of process parameters on the *SCE*: a) – *I*, b) – *SCE* versus *D*, c) – *SCE* versus *f*,
d) – *SCE* versus *S*

As shown in Fig. 12a, it can be stated that the R_a is decreased 20.4% with an increment in the *I* (from 20 to 35 deg.). A further *I* (from 35 deg. to 50 deg.), the R_a is increased by around 20.8%. An increment in the inclined angle leads to a reduction in the turning area; hence, the material volume decreases. A small amount of the material is removed and the surface roughness decreases. A further angle increases the turning area, leading to a higher material volume to be cut. The material is hardly turned; hence, the R_a increases.

As shown in Fig. 12b, it can be stated that the R_a is increased by 24.9% with an increment in the *D* (from 0.2 to 0.6 mm). A higher *D* increases the material removal volume to be cut and a high amount of the material is turned; hence, the surface roughness increases. Additionally, a higher pressure leads to greater friction between the turning insert and the workpiece. The material is hardly processed and the R_a increases.

As shown in Fig. 12c, it can be stated that the R_a is increased by 40.9% with an increment in the *f* (from 0.3 to 0.7 mm/rev). A higher *f* increases the distance between two successive paths; leading to higher chip thickness. Higher material volume is removed, leading to an increment in the feed marks; hence, the roughness increases. Additionally, a higher *f* may cause an increased strain-hardening behaviour because of higher machining forces. This leads to unstable machining force; hence, the R_a increases.
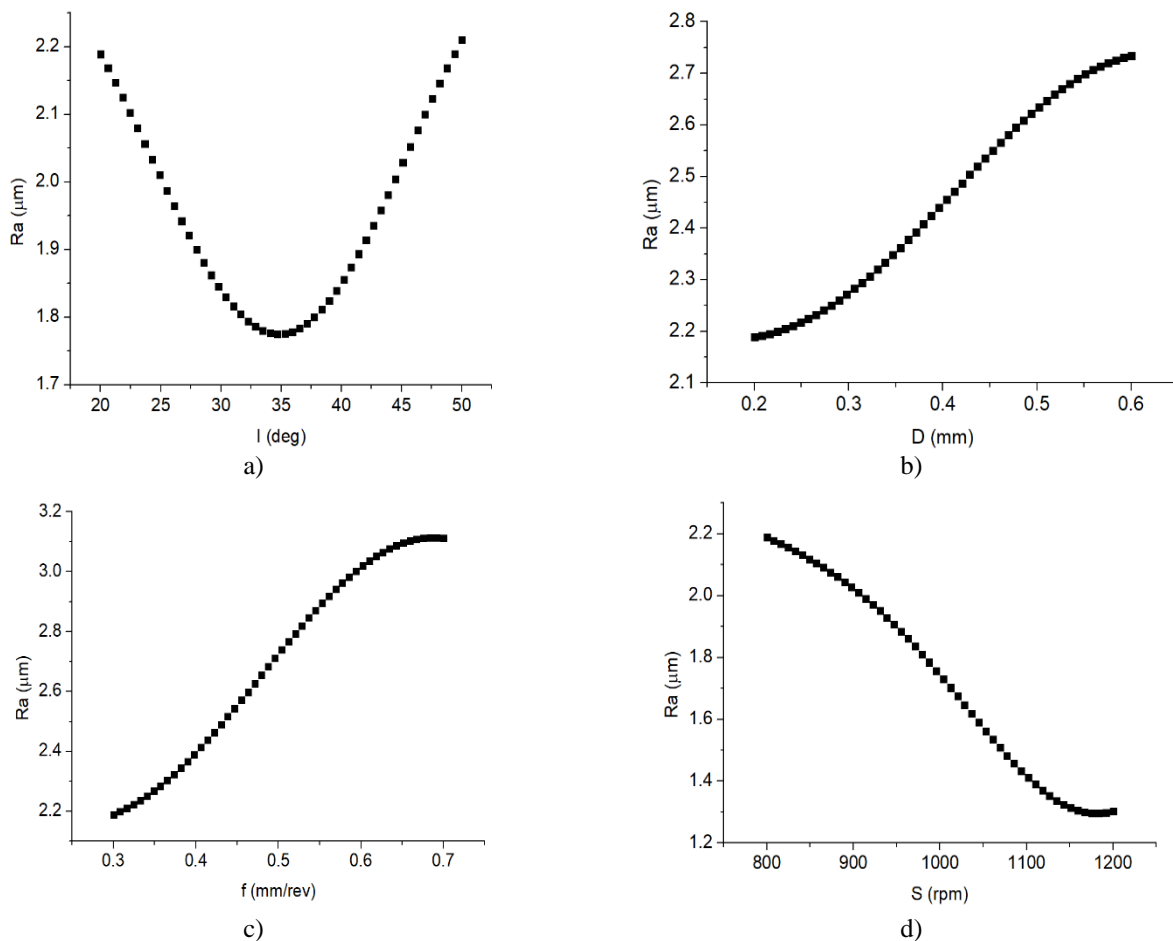
Fig. 12. The impacts of process parameters on the R_a: a) – R_a versus I, b) – R_a versus D, – c) R_a versus f, d) – R_a versus S

As shown in Fig. 12d, it can be stated that the R_a is decreased by 41.6% with an increment in the S (from 800 to 1200 rpm). A higher S causes an increase in the temperature of the cutting region, leading to reductions in the strength and hardness of the workpiece. The material is softly turned; hence, the R_a decreases. Additionally, a higher S may reduce the vibration, resulting in a stable turning; hence, a low R_a is obtained.

4.4. OPTIMIZING OUTCOMES PRODUCED BY THE VCPSO

Table 9 presents the normalized values for computing turning responses. Table 10 lists the entropy and weight values for the technical responses. As a result, the weight values of the SCE and R_a are 0.81 and 0.06, respectively.

The Pareto graph generated by VCPSO is depicted in Fig. 13. It can be stated that machining performances have contradictory trends. The minimization of the average roughness leads to an increment in the specific cutting energy.

As a result, the optimum findings of the I, D, f, and S are 35 deg., 0.45 mm, 0.50 mm/rev., and 1200 rpm, respectively (Table 11). The reductions in the SCE and R_a are 37.4% and 6.6%, respectively, as compared to the initial values.

Table 9. Normalized values of the turning responses

Normalized response		$p_{ij} \times \ln p_{ij}$	
SCE	R_a	SCE	R_a
0.02928	0.03574	0.10339	0.11906
0.02555	0.04538	0.09369	0.14034
0.05123	0.03574	0.15223	0.11906
0.02222	0.04721	0.08458	0.14413
0.01984	0.03507	0.07777	0.11751
0.01617	0.04621	0.06670	0.14208
0.04817	0.03590	0.14611	0.11945
0.06509	0.03906	0.17783	0.12666
0.05306	0.03374	0.15581	0.11436
0.02324	0.04704	0.08742	0.14379
0.06006	0.03707	0.16892	0.12214
0.02799	0.04754	0.10010	0.14482
0.03880	0.04787	0.12607	0.14549
0.03071	0.03607	0.10697	0.11984
0.02120	0.03225	0.08170	0.11075
0.03717	0.04854	0.12236	0.14685
0.04301	0.03674	0.13532	0.12137
0.02466	0.04771	0.09132	0.14516
0.03268	0.03457	0.11180	0.11633
0.04457	0.02261	0.13865	0.08567
0.05286	0.02427	0.15541	0.09024
0.03078	0.03574	0.10714	0.11906
0.06190	0.03840	0.17222	0.12517
0.02561	0.04837	0.09387	0.14651
0.03051	0.03590	0.10646	0.11945

Table 10. The Entropy value and weight for responses

Criteria	SCE	Ra
Entropy value	0.97337	0.99390
Dispersion value	0.02663	0.00610
Weight	0.81	0.19

Table 11. The results produced by the VCPSO

| Method	I (deg.)	D (mm)	f (mm/rev.)	S (rpm)	SCE (J/mm³)	Ra (μm)
Initial values	35	0.40	0.4	1000	5.64	1.97
Optimal values	35	0.45	0.5	1200	3.53	1.84
Reductions (%)					37.4	6.6
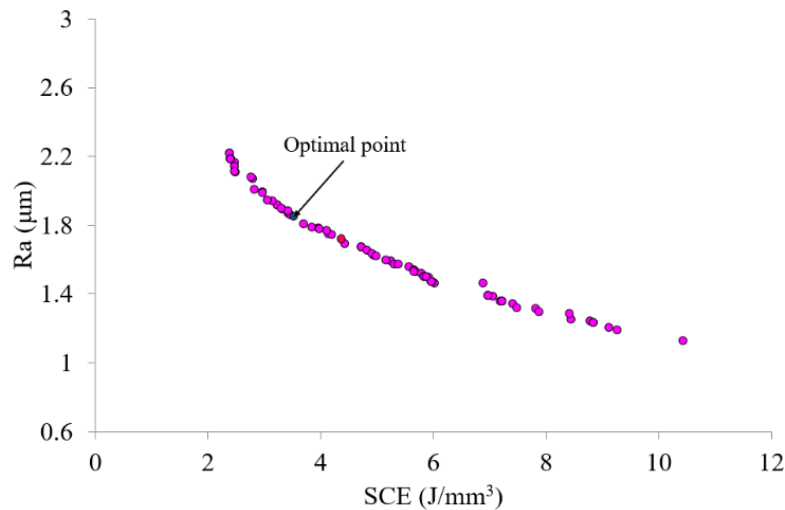
Fig. 13. The Pareto fronts generated by VCPSO

4.5. EVALUATION OF THE TOTAL TURNING COST

The comprehensive model for the cost of the HRT process (*TC*) is expressed as:

$$TC = C_E + C_L + C_C + C_F + C_M + C_N \tag{20}$$

where C_E, C_L, C_C, C_M, and C_N present the cost of energy consumed, the cost of the turning tool, the cost of the labor, the cost of the tool change, the cost of the lubricant, the cost of the machine degradation and remanufacturing, and the cost of the machining noise, respectively.

The C_E is computed as:

$$C_E = k_e EC \tag{21}$$

where k_e is the energy cost.

The C_T is computed as:

$$C_T = k_c \frac{t_c}{T_T} \tag{22}$$

where k_c and T_T are the cost of the turning tool and tool life, respectively. The T_T is expressed as:

$$T_T = \frac{A}{V^\alpha f^\beta d^\gamma} \tag{23}$$

where A, α, β, and γ are the experimental coefficients.

The C_L is computed as:

$$C_L = k_{labor}(t_o + t_{st} + t_a + t_{ch} + t_c) \tag{24}$$

where k_{labor} presents the labor cost.

The C_C is computed as:

$$C_C = k_{labor} t_{ch} \frac{t_c}{T_T} \tag{25}$$

The C_F is computed as:

$$C_F = \frac{(k_{fp} + k_{fd})(t_o + t_{st} + t_a + t_{tc} + t_c)V_u}{T_L}$$ (26)

where V_u, k_{fp}, and k_{fd} are the volume consumed of the lubricant, the cost for the lubricant preparation, the cost for the lubricant disposal, respectively.

The C_M is computed as:

$$C_M = \frac{(k_{md} + k_{mr})(t_o + t_{st} + t_a + t_{ch} + t_c)}{T_m}$$ (27)

where k_{md}, k_{mr}, and T_m are the cost of the machine degradation, the cost of the machine remanufacturing, the service life of the machine, respectively.

The C_N is computed as:

$$C_N = \frac{k_n(t_o + t_{st} + t_a + t_{tc} + t_c)}{T_W}$$ (28)

where k_n and T_w are the noise tax and the number of working hours per month, respectively.

Table 12 presents the coefficients of the *TC* model. As a result, the *TC* is decreased by 7.5% at the optimal solution (Table 13).

Table 12. Coefficients for the rotary turning operation

k_e (USD/kWh)	k_c (VND/piece)	A	α	β	t_o (s)	t_{st} (s)	t_a (s)	t_{ch} (s)
0.15	16.62	16.2×10^5	2.65	0.27	4	6	8	8
k_{labour} (USD/h)	V_u (l)	k_{fp} (USD/l)	k_{fd} (USD/l)	T_L (month)	k_{md} (USD)	k_{mr} (USD)	T_W (year)	k_n (USD)
8.4	20	0.14	0.45	1	41244.8	1649.8	14	2.68

Table 13. Comparative values of the total cost

Method	Optimization parameters				Response
	I (deg.)	D (mm)	f (mm/rev.)	S (rpm)	TC (USD)
Initial values	35	0.40	0.4	1000	4.52
Optimal results	35	0.45	0.5	1200	4.18
Reduction (%)					7.5

4.6. THE CONTRIBUTION ANALYSIS

The designed and fabricated self-propelled rotary tool could be used for machining difficult-to-cut materials. This device is a significant reference for developing other self-propelled rotary tools.

The optimal data could be applied to the practical HRT process to decrease the specific cutting energy and surface roughness.

The *SCE* and R_a models could be utilized to predict the response outcomes for machining the mold steel entitled SKD61.

The developed HRT process could be employed for machining other hardened steels.

The proposed technique could be used to solve optimization issues for other machining processes.

The proposed model of the total cost could be applied to estimate the rotary turning expenses.

5. CONCLUSIONS

In the current study, the specific cutting energy (*SCE*) and average roughness (*R_a*) of the HRT process were reduced using optimal data of the inclined angle (*I*), depth of cut (*D*), feed rate (*f*), and spindle speed (*S*). The BRFFNN-assisted models were applied to propose the *SCE* and *R_a*. The entropy approach and VCPSO were applied to determine optimizing outcomes. The findings are listed below:

1. To Save the *SCE*, the middle value of the *I* could be applied, while low *D*, *f*, and *S* were recommended. To reduce the *R_a*, the low *D* and *f* were employed, while the high *I* and *S* were applied.

2. For the *SCE* model, the depth of cut was named as the most effective parameter, followed by the feed rate, spindle speed, and inclined angle, respectively. For the *R_a* model, the spindle speed had the highest contribution, followed by the feed rate, depth of cut, and inclined angle, respectively.

3. The optimal outcomes of the *I*, *D*, *f*, and *S* were 35 deg., 0.45 mm, 0.40 mm/rev., and 1200 rpm, respectively. The reductions in the *SCE* and *R_a* were 37.4% and 6.6%, respectively.

4. The total cost of the HRT process could be saved around 7.5% at the optimal solution.

5. The impacts of HRT factors on air pollution and noise emission have been not analysed. A holistic optimization will be performed to consider more environmental metrics.

REFERENCES

[1]   DESSOLY V., MELKOTE S.N., LESCALIER C. 2004, *Modeling and Verification of Cutting Tool Temperatures in Rotary Tool Turning of Hardened Steel*, Int. J. Mach. Tools Manuf., 44, 1463–1470.

[2]   KISHAWY H.A., WILCOX J., 2003, *Tool Wear and Chip Formation During Hard Turning with Self-Propelled Rotary Tools*, Int. J. Mach. Tools Manuf., 43, 433–439.

[3]   KISHAWY H.A., PANG L., BALAZINSKI M., 2011, *Modeling of Tool Wear during Hard Turning with Self-Propelled Rotary Tools*, Int. J. Mech. Sci., 2011, 53, 1015–1021.

[4]   KISHAWY H.A., BECZE C.E., MCINTOSH D.G., 2044, *Tool Performance and Attainable Surface Quality During the Machining of Aerospace Alloys Using Self-Propelled Rotary Tools*, J. Mater. Process. Technol., 152, 266–271.

[5]   WANG S.H., ZHU X., Li X., TURYAGYENDA G., 2006, *Prediction of Cutting Force for Self-Propelled Rotary Tool Using Artificial Neural Networks*, J. Mater. Process. Technol., 180, 23–29.

[6]   LI L., KISHAWY H.A. 2006, *A Model for Cutting Forces Generated During Machining with Self-Propelled Rotary Tools*, Int. J. Mach. Tools. Manuf., 46, 1388–1394.

[7]   EZUGWU E.O., 2207, *Improvements in The Machining of Aero-Engine Alloys using Self-Propelled Rotary Tooling Technique*, J. Mater. Process. Technol., 185, 60–71.

[8]   RAO T.B., KRISHNA A.G., KATTA R.K., KRISHNA K.R. 2015, *Modeling and Multi-Response Optimization of Machining Performance While Turning Hardened Steel with Self-Propelled Rotary Tool*, Adv. Manuf., 3, 84–95.

[9]   AMINI S., TEIMOURI R., 2017, *Parametric Study and Multicharacteristic Optimization of Rotary Turning Process Assisted by Longitudinal Ultrasonic Vibration*, Proc. Inst. Mech. Eng. E: J. Process Mech. Eng., 231/5, 978–991.

[10]   NGUYEN T.T., 2020, *An Energy-Efficient Optimization of the Hard Turning Using Rotary Tool*, Neural Comput. & Applic., 33, 2621–2644.

[11]   NGUYEN T.T., DUONG Q.D., MIA M., 2020, *Sustainability-Based Optimization of the Rotary Turning of the Hardened Steel*, Metals, 10, 939.

[12]   UMER U., KISHAWY H., ABIDI M.H., MIAN S.H., MOIDUDDIN K., 2020, *Evaluation of Self-Propelled Rotary Tool in the Machining of Hardened Steel using Finite Element Models*, Materials, 13, 5092.

[13]   AHMED W., HEGAB H., MOHANY A., KISHAWY H., 2021, *Analysis and Optimization of Machining Hardened Steel AISI 4140 with Self-Propelled Rotary Tools*. Materials, 14, 6106.

[14]   NIESLONY P., KROLCZYK G., CHUDY R., WOJCIECHOWSKI S., MARUDA R., BILOUS P., LIPOWCZYK M., STACHOWIAK L., 2020, *Study on Physical and Technological Effects of Precise Turning with Self-Propelled Rotary Tool*, Precis. Eng., 66, 62–75.

[15]   THELLAPUTTA G.R., BOSE P., RAO C., RAJU C., 2019, *Effect of Machining Variables on Cutting Temperature While Rotary Milling of Inconel 625*, Recent Advances in Material Sciences, 27–36.

[16]   AHMED W., HEGAB H., KISHAWY H., MOHANY A., 2021, *Estimation of Temperature in Machining with Self-Propelled Rotary Tools Using Finite Element Method*, J. Manuf. Process., 61, 100–110.

[17]   AHMED W., HEGAB H., MOHANY A., KISHAWY H., 2021, *On Machining Hardened Steel AISI 4140 with Self-Propelled Rotary Tools: Experimental Investigation and Analysis*, Int. J. Adv. Manuf. Technol., 113, 3163–3176.

[18]   UMER U., MIAN S.H., MOHAMMED M.K., ABIDI M.H. MOIDUDDIN K., KISHAWY H., 2022, *Self-Propelled Rotary Tools in Hard Turning: Analysis and Optimization via Finite Element Models*, Materials, 15/24, 8781.

[19]   TRUNG D.D., 2021, *Application of TOPSIS an PIV Methods for Multi – Criteria Decision Making in Hard Turning Process*, Journal of Machine Engineering, 21/4, 57–71, https://doi.org/10.36897/jme/142599.

[20]   NGUYEN A., NGUYEN V., LE T., NGUYEN N., 2023, *A Hybridization of Machine Learning and NSGA-II for Multi-Objective Optimization of Surface Roughness and Cutting Force in ANSI 4340 Alloy Steel Turning*, Journal of Machine Engineering, 23/1, 133–153, https://doi.org/10.36897/jme/160172.